


Article

Shrinkage Cracking of Concrete Slabs-On-Grade: A Numerical Parametric Study

Giuseppe Tiberti ^{1,*} , Antonio Mudadu ¹, Bryan Barragan ² and Giovanni Plizzari ¹

¹ Department of Civil, Environmental, Architectural Engineering and Mathematics, University of Brescia, 25123 Brescia, Italy; a.mudadu@unibs.it (A.M.); giovanni.plizzari@unibs.it (G.P.)

² Infrastructure Solutions, Owens Corning, 73000 Chambéry, France; bryan.barragan@owenscorning.com

* Correspondence: giuseppe.tiberti@unibs.it; Tel.: +39-030-371-1221

Received: 18 August 2018; Accepted: 3 September 2018; Published: 5 September 2018



Abstract: Industrial pavements are thin slabs on a continuous support subjected to restrained shrinkage and loads. The use of fibers as an alternative reinforcement to steel welded wire mesh and rebars is today an extensive practice for the reinforcement of concrete slabs-on-grade. Despite the widespread use of fiber reinforcement, the corresponding benefits in controlling cracking phenomena due to shrinkage are generally not considered in the design process of Fiber Reinforced Concrete (FRC) slabs-on-grade. The post-cracking performance provided by glass macro-fibers at low crack openings is particularly convenient in structures with a high degree of redundancy. Referring to service conditions, it is well known that concrete shrinkage as well as thermal effects tend to be the principal reasons for the initial crack formation in slabs-on-grade. A numerical study on the risk of cracking due to shrinkage in ground-supported slabs is presented herein. Special attention is devoted to the evaluation of the beneficial effects of glass fibers in controlling cracking phenomena due to shrinkage. The numerical analyses are carried out on jointless pavements of different sizes. Since shrinkage stresses in slabs-on-grade are considerably influenced by external constraints which limit the contractions, different subgrade conditions have been also considered.

Keywords: pavements; glass fibers; shrinkage phenomena; subgrade conditions; non-linear analyses; curling

1. Introduction

Industrial pavements and floors are thin slabs on a continuous support and they are wrongly considered non-structural or secondary structures. Although international design guidelines for slabs-on-grade are now available [1–4], in many countries there are not mandatory rules for industrial pavements. As a consequence, the industrial floors often evidence several pathologies that take place during construction and service conditions that brings owners, construction companies, and designers to legal disputes [5].

The main problems found in industrial floors are related to extensive crack phenomena that often occurs before applying the service loads on the pavement. These cracks are generally due to shrinkage effects (and, in some cases, the thermal effects) that mainly develop during the first few weeks after concrete pouring (due to the large size and exposed surface, low thickness, and high degree of restraint). To the contrary, if shrinkage cracks do not early appear, shrinkage stresses will represent an additional contribution to the load effect and may favor cracking phenomena when loads are applied.

Moreover, the differential shrinkage along the thickness of the slab leads to upward curling on the edges of the slab [6–9]. Curling of concrete slabs-on-grade remains a major concern and its mitigation is critical for crack control, durability, and mechanical performance [10–13]. In fact, cracks due to shrinkage phenomena need to be repaired by means of typical measures such as the

replacement of the cracked portion with epoxy grouting, besides cutting more joints [14], leading to high maintenance costs.

Industrial slabs-on-grade could be designed with contraction joints or joints-free (e.g., jointless, reducing the construction and maintenance costs). In the latter case the ground-supported slabs are more exposed to shrinkage phenomena, which can be limited by means of post tensioning [15,16] or shrinkage-compensating concrete. In addition, enhanced materials, such as Fiber Reinforced Concretes (FRCs) can be adopted, since they enable the formation of a large number of micro-cracks instead of few macro-cracks as a result of their noticeable post-cracking residual strengths. Nevertheless, the benefits for shrinkage cracking due to FRC are generally not considered in the design process of FRC ground-supported slabs since the attention is mainly devoted to the replacement of conventional reinforcement.

Short, randomly and homogeneously distributed fibers allow elimination of critical phases of the floor construction process [5,17–20]. Fibers guarantee a homogeneous and three-dimensional reinforcement, improving crack control during the whole lifespan of the concrete floor [21,22]. In addition, fibers significantly enhance fatigue resistance of concrete [23–25], which is particularly important for these structures.

The relatively high post-cracking performance provided by glass macro-fibers at low crack openings is particularly convenient for highly statically redundant structures such as slabs on grade [5], both at Serviceability Limit State (SLS, due to shrinkage phenomena) and Ultimate Limit State (ULS), when the ultimate capacity still involves very low crack openings (usually below 0.3 mm).

Within this framework, in order to evaluate the effect of glass macro-fibers in slabs-on-grade with shrinkage phenomena, a parametric study based on non-linear numerical analyses was carried out by considering different slab geometries and distributions of shrinkage deformations along the slab thickness; subgrade friction was investigated as well. Jointless pavements without contraction joints were considered in order to evaluate if glass fiber reinforcement can mitigate cracking phenomena even when rather large distances between construction joints are used. In this regard, the relatively simple numerical model and results obtained represent reliable and useful tools for designers and practitioners, since they provide the main information for evaluating the risk of cracking in jointless pavements reinforced by glass fibers under shrinkage phenomena.

2. Slab Geometry and Investigated Parameters

Jointless pavements are, by definition, pavements without contraction joints. The latter consist of sawed, formed, or tooled grooves in a concrete slab, which create weakened vertical planes, expected to localize cracking phenomena caused by general dimensional changes in the slab (e.g., shrinkage or thermal effects). Therefore, in jointless pavements only construction joints are present.

The growing interest in jointless pavement is related to the noticeable reduction of damage produced by wheels crossing contraction joints, reduced construction time and cost, as well as maintenance expenses. Nevertheless, the risk of cracking due to shrinkage phenomena as well as the main parameters affecting this phenomenon are still matters of discussion within the scientific community. In this regard, the main factors under investigation in the numerical parametric study presented herein are

1. Slab dimensions;
2. Subgrade properties;
3. Material properties;
4. Shrinkage development.

2.1. Slab Dimensions

A typical square-shaped portion of jointless ground-supported slab having a thickness of 180 mm was adopted as reference. By assuming a maximum concrete casting volume per day of about 200 cubic meters, the following two slab dimensions were considered:

- 20 × 20 m;
- 30 × 30 m.

The mutual interaction of the pavement portion under investigation and those neighboring depends, most of all, on the type of construction joints adopted (e.g., joints with dowel bars of different forms) but also on the sequence in time used for casting day-by-day the whole concrete pavement. Hence, for the sake of simplicity, the aforementioned interaction has been neglected by considering the four sides of the square slab as free edges.

2.2. Subgrade Properties

The slabs-on-grade performance under static loads strictly depends on the flexural slab stiffness (e.g., slab thickness) and on the mechanical properties of the ground. The latter, in practice, are considered by designers by means of simplified methods. The most commonly used is the Winkler model, which only takes into account the equivalent elastic stiffness exhibited by the ground in presence of vertical displacements perpendicular to the middle-slab-plane (Winkler soil stiffness, $K_{Winkler}$).

The slab-on-grade behavior under shrinkage is principally related to the interfacial friction between slab and supporting base [10]. It is noteworthy that this local frictional behavior must be described by means of a proper resistance criteria (e.g., Mohr Coulomb or Drucker-Prager) but especially through an adequate stress–slippage friction relationship, which defines the phenomena from a kinematic point of view [10,11].

A number of experimental studies [26–28] have stated that the development of interfacial friction stresses and slippage at the base of the slab can be described by a bilinear function (as shown in Figure 1). In fact, the shear friction stresses almost linearly increase to a certain value (δ_0, τ_0) with the increase of slab slippage; afterwards, the stresses develop according to an ideal-perfect-plastic constant branch. The main subgrade parameters considered are listed in Table 1. It can be noticed that, in order to simplify the comparison of results, a unique reference value of Winkler soil stiffness was used ($K_{Winkler} = 0.08 \text{ N/mm}^3$), which was obtained by averaging the typically $K_{Winkler}$ values used for loose sand (0.04 N/mm^3) and clayed soil (0.12 N/mm^3).

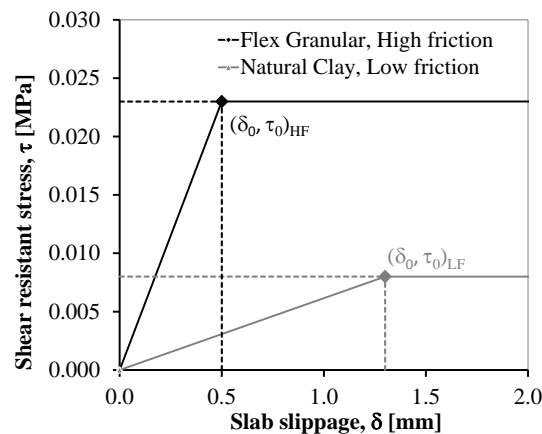


Figure 1. Bilinear friction stress vs. slab slippage relationship, Wimsatt et al. [27].

Table 1. Main subgrade parameters concerning its stiffness and its frictional behavior.

Subgrade	$K_{Winkler}$ (N/mm^3)	Frictional Behavior	
		τ_0 (MPa)	δ_0 (mm)
Low friction, LF	0.08	0.008	1.3
High friction, HF	0.08	0.023	0.5

2.3. Material Properties

Concrete reinforced with glass macro-fibers (Glass-FRC) with a strength class C35/45 (according to Eurocode 2 [29]) was considered. Glass fibers having a length (L_f) of 36 mm, a diameter (φ_f) of 0.54 mm, and an aspect ratio (L_f/φ_f) equal to 67 were used. These fibers are high-performance alkali-resistant glass macro-fibers with a filament tensile strength (f_{uf}) higher than 1700 MPa and an elastic modulus of 72 GPa. Two fiber contents were selected: 5 kg/m³ and 10 kg/m³, corresponding to a volume fraction (V_f) of 0.19% and 0.38%, respectively. The mixture proportion (by weight) of both Glass-FRC05 and Glass-FRC10 was 1:2.88:3.44:0.58:0.01 for 300 kg/m³ of CEM I 52.5R cement: sand (0–4 mm): gravel (4–20 mm): water: super-plasticizer. Both mixtures exhibited a good and comparable workability. Six cube specimens (150 mm side) were cast for measuring the compressive strength and six small beams (150 × 150 × 550 mm) were prepared for the evaluation of the Glass-FRC flexural performance according to EN 14651 [30]. Table 2 reports the mechanical properties of concrete: 28-days cubic ($f_{cm,cube}$) and cylindrical (f_{cm}) mean compressive strength. The mean cylindrical tensile strength (f_{ctm}) is reported as well. The latter was estimated from the equation reported in Eurocode 2 [29]: $f_{ctm} = 0.3 \cdot f_{ck}^{2/3}$. The characteristic compressive strength of concrete was evaluated according to: $f_{ck} = f_{cm} - 8$ MPa [29]. Similarly, the concrete elastic modulus (E_c) was evaluated by means of the relationship: $22 \cdot (f_{cm}/10)^{0.3}$ [29]. The cylindrical compressive strength, as a first approximation, was estimated as $f_{cm} = 0.83 \cdot f_{cm,cube}$.

Figure 2 exhibits the mean experimental nominal stress vs. CMOD (Crack Mouth Opening Displacement) of Glass-FRC05 and Glass-FRC10 [30]. The limit of proportionality (f_{Lm}) and the values of the average residual flexure tensile strengths (f_{R1m} , f_{R3m} , corresponding to CMOD values of 0.5 mm and 2.5 mm, respectively), are listed in Table 2.

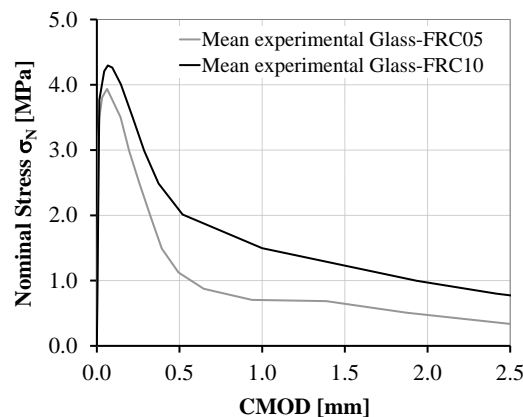


Figure 2. Nominal stress–CMOD mean experimental curves according to EN14651 [30].

Table 2. Mean mechanical properties of Glass-FRCs.

Batch ID	E_c ¹	$f_{cm,cube}$	f_{cm} ¹	f_{ctm} ¹	f_{Lm}	f_{R1m}	f_{R3m}
	(MPa)	(MPa)	(MPa)	(MPa)	(MPa)	(MPa)	(MPa)
Glass-FRC05	33.9	50.6	42.0	3.16	3.93	1.11	0.34
Glass-FRC10	33.9	50.8	42.2	3.16	4.27	2.04	0.78

¹ Estimated from $f_{cm,cube}$.

2.4. Shrinkage Development

Shrinkage of concrete is a physical property caused by a loss in volume. The main factors affecting this phenomenon are the ambient temperature and humidity, the dimensions of the element, and the composition of the concrete and its curing procedure.

Several shrinkage laws are proposed in literature [29,31–34]. Among them, in Eurocode 2 [29] a simple free-shrinkage model is reported, where the total deformation corresponds to the addition of two components: autogenous and drying shrinkage ($\varepsilon_a(t)$ and $\varepsilon_d(t)$, respectively). In order to better compare the results a unique reference free-shrinkage-law has been adopted; therefore the Eurocode 2 free-shrinkage model [29] was applied according to the following parameters:

- conventional notional sizes (h_0) equal to 100 mm;
- ambient relative humidity of 65%;
- curing time equal to 7 days;
- cement class R [29].

As a first approximation, a unique h_0 was considered herein, independently of the slab dimensions investigated. In this regard, the most conservative value for h_0 suggested by Eurocode 2 [29] has been used. The development of shrinkage strain is depicted in Figure 3a.

Shrinkage of concrete characterizes the entire structural behavior of the slab, inducing typical curling phenomena. The latter is principally caused by a non-uniform distribution of shrinkage deformations along the slab thickness. In fact, the drying shrinkage of a concrete slab is non-uniform because of the different moisture and evaporation conditions at the surface and base of the slab. Regarding the distribution of shrinkage deformation along the slab thickness, only few experiences are reported in literature. In an early study, Rasmussen & McCullough [35] assumed that the full shrinkage appears at the surface of a concrete pavement and no shrinkage occurs below the mid-depth of the slab. The shrinkage was assumed to decrease in a linear manner between the top and center of the slab. Heath & Roesler [36] assessed the distribution of drying shrinkage by using strain gauges installed at various locations on full-scale slabs-on-grade. The gauges were installed near the top or bottom of the slabs at the corner, edge, or center. All the instrumented slabs were 200 mm thick. The Authors [36] stated a considerable scatter in the data and, as a result, no noticeable difference in data for the center, edge, or corner of the slabs, or for the long or short slabs, could be identified. On the other hand, the only identifiable difference was that between the top and bottom of the slab, as shown in Figure 3b.

It can be noticed that drying shrinkage deformations are not negligible at the bottom surface of the slab. The percentage ratios between shrinkage strains exhibited at bottom and top surface are also reported (Figure 3b); the average value of this ratio (equal to 60%) is evidenced as well.

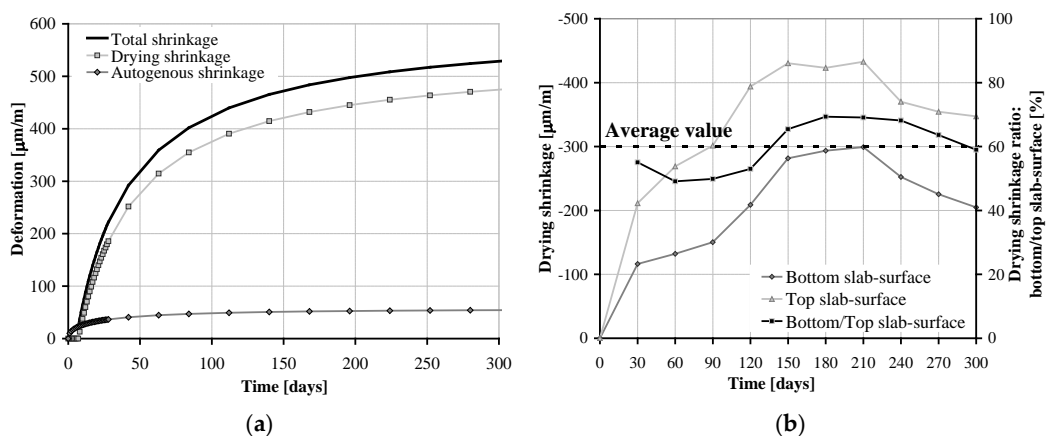


Figure 3. (a) Shrinkage strain vs time according to Eurocode2 [29]; (b) average distribution of drying shrinkage along the slab thickness according to Heath&Roesler [36].

The autogenous shrinkage depends principally on the cement hydration and occurs during hardening phase of concrete. Hence, it can be probably considered uniform along the slab thickness, with limited effects on curling phenomenon in spite of a considerable influence on the slab shortening.

Three possible scenarios of shrinkage distribution along slab thickness were considered in the present work, as schematically depicted in Figure 4. Each distribution assumes full-shrinkage of the top-slab surface and induces a different imposed curvature to the slab together with a specific axial shortening.

The scenario defined as Linear 01 (abbreviated as Lnr01) was based on the drying shrinkage data reported in [36] and it will be considered as the reference one; a ratio between bottom and top slab-surface deformation $\varepsilon_{d,bottom}(t)/\varepsilon_{d,top}(t)$ equal to 50% was assumed according to a linear distribution. Besides configuration Lnr01, the uniform case (defined as Unifr) aims at an ideal favorable condition where no curling-effects are considered, while Linear 02 (Lnr02) results in a severe situation with a considerable imposed curvature to slab-sections ($\varepsilon_{d,bottom}(t)/\varepsilon_{d,top}(t)$ equal to 25%).

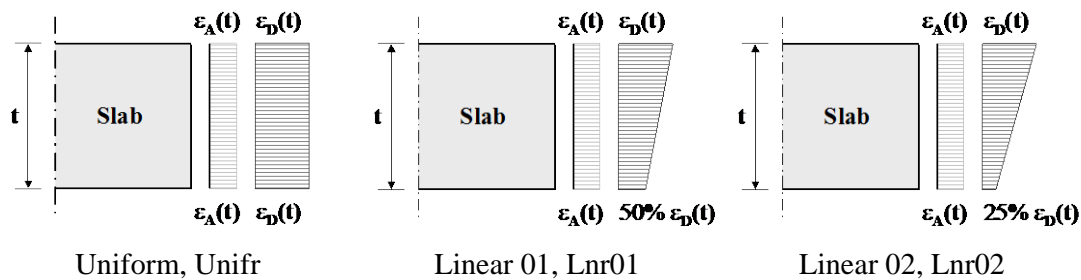


Figure 4. Autogenous and drying shrinkage distributions under investigation.

3. Numerical Modeling

The determination of stress and strain fields in concrete slabs-on-grade with shrinkage phenomena can be performed by using simplified analytical methods [10,11], which generally refer to ideal slab configurations (e.g., rectangular slab, uniform shrinkage distribution along the thickness or concrete assumed as linear-elastic material). Even if these analytical models are valuable for getting basic information, they cannot completely describe the behavior of a square concrete slab-on-grade, especially in the cracked stage. Nowadays, in spite of the several available numerical approaches [13,37–39], there is still a lack of relatively simple numerical models aiming at taking into account both the concrete post-cracking behavior and the frictional effects at the contact surface between the slab and the subgrade.

The research work presented herein is focused on the behavior of Glass-FRC slabs-on-grade after cracking, during shrinkage development. To this aim, opportune numerical models of concrete cracking have to be used in order to properly include the residual strength provided by fibers after cracking and to evaluate the consequent improvement of crack control, which plays a key role for the durability of the structure. Moreover, particular attention was devoted to the simulation of the slab-to-subgrade frictional behavior.

3.1. Numerical Modeling of Materials

The numerical analyses were performed by means of the finite element program DIANA (9.4.4, DIANA FEA BV, Delft, The Netherlands) [40]. A smeared crack approach has been used to describe a crack pattern having cracks on an arbitrary location [41]. The multi directional fixed crack model was adopted, which is based on the decomposition of the total strain into an elastic and a crack strain [40]. The latter is introduced since the crack is considered to be spread over an area that belongs to an integration point of the mesh. Concrete in tension was assumed to be linear up to f_{ctm} . The post-cracking uni-axial tensile law for FRCs proposed by Model Code 2010 [34], was adopted (Figure 5), which is defined through the flexural residual strength values, determined from bending tests on notched prisms according to EN 14651 [30]. Based on the mean values of post-cracking residual strengths listed in Table 2, the main parameters of the Glass-FRCs tensile law were calculated, as reported in Figure 5. It is worth noticing that, when referring to finite element (FE) models based on smeared crack approach, a proper internal length (L_i) should be evaluated [42]. The latter depends

on the cracking model implemented in the program; hence, L_i is not a property of the structure but it represents a “numerical parameter”, which enables, as a first approximation, to easily connect continuum mechanics, governed by a stress–strain constitutive relationship, and fracture mechanics, governed by a stress-crack opening law, initially proposed by Hillerborg et al. [43]. According to Rots [41], L_i corresponds to the average element dimension.

The uni-axial compressive response of concrete was considered as linear elastic up to f_{cm} (based on data reported in Table 2, a unique f_{cm} was assumed equal to 42.1 MPa) and subsequently as ideal-plastic. More detailed compressive laws were useless since, as expected, in all numerical simulations concrete compressive stresses remained within the elastic limit.

The three shrinkage distributions along the slab thickness previously described (Figure 4) were numerically simulated by considering fictitious temperature distributions along the slab thickness. Based on the thermal expansion coefficient, a specific time-history of temperatures is imposed in order to apply a time-history of shrinkage deformations. By using this approach, the shrinkage distribution as well as its development (in-time) can be easily customized with a relatively simple method. Creep and relaxation were not considered in the numerical model, since they generally tend to reduce the magnitude of the tensile stresses and, consequently, the probability of cracking; similarly, the possible additional stresses due to restrained creep and relaxation deformations, as result of the existence of fibers, were assumed negligible within the framework of the relatively simple numerical model proposed herein.

It should be noticed that, as a first approximation, the concrete mechanical properties as well as the post-cracking strengths were not time-dependent. This simplified assumption is acceptable since, as it will be discussed in Section 4, in most of the analyses carried out cracks do not appear at early age. In addition, a curing time equal to seven days was assumed for all the analyses, leading to rather limited shrinkage effects during this initial period. Moreover, it is well known that in the initial seven curing days, the concrete mechanical properties rapidly increase reaching almost eighty percent of 28-days strengths.

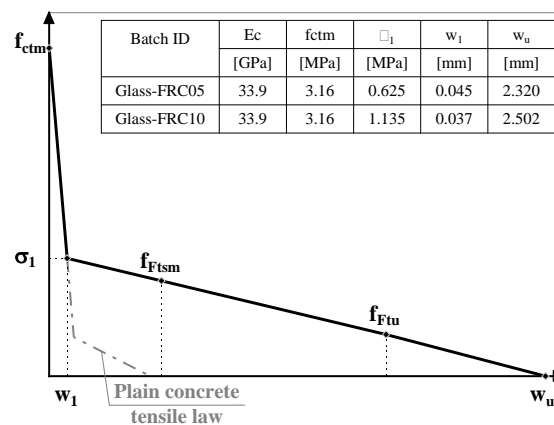


Figure 5. Scheme of uni-axial post-cracking behavior of Glass-FRC evidencing parameters.

3.2. Slab-On-Grade Numerical Model

The square shaped portion of a jointless slab of 180 mm thickness was simulated as a slab on continuum support. Only one quarter of the investigated portion of pavement was analyzed with the FE program, by taking advantage of the symmetry (Figure 6a). In fact, it was assumed to apply the dead weight of the pavement and, afterwards, the shrinkage deformations were progressively imposed by means of a time-steps analysis. In other words, the applied dead-load and shrinkage deformations are spatially uniform along the slab. On the other hand, as mentioned before, shrinkage deformation varies along the slab thickness (Figure 4).

The pavement was modelled by means of eight-nodes quadrilateral isoparametric shell elements [44], able to properly take into account the concrete post-cracking non-linear behavior. The definition of the size of the finite elements is an important point regarding the model. In this regard, preliminary non-linear numerical analyses (taking into account the post-cracking behavior) with different mesh-refinements were carried out. It should be noticed that, in this preliminary stage, the analyses were also developed by using models based on continuum brick elements. Eventually, for achieving a balance between computational time and reliability of results, a regular mesh was chosen with shell elements having a side of 200 mm. Hence, based on Rots [40,41], L_i was considered equal to 200 mm.

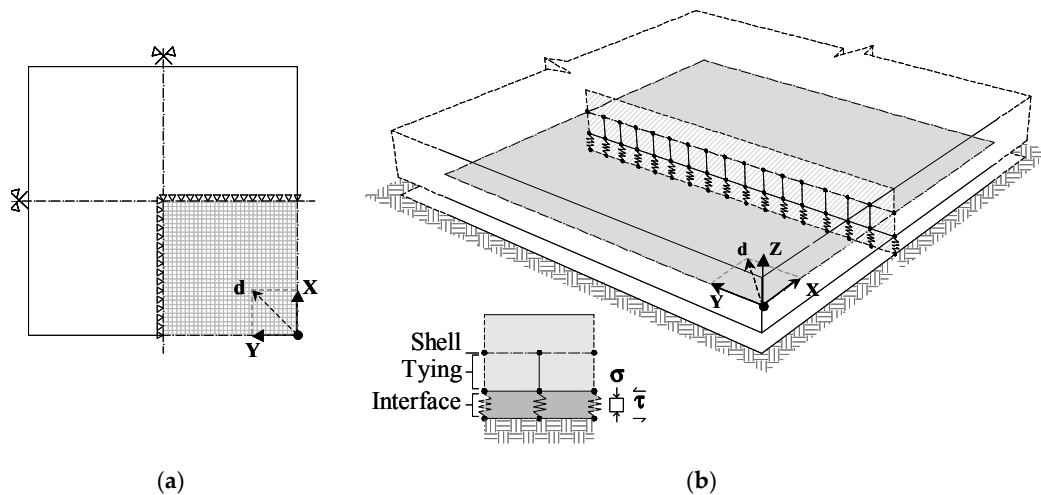


Figure 6. (a) Top view of the mesh adopted; (b) simplified scheme of the model adopted.

In order to properly model the stiffness of the subgrade as well as its frictional interaction with the above pavement, eight nodes quadrilateral interface elements were used. The interface elements principally consist of two parallel planes which can exhibit relative in-plane displacement (slippage) or relative out-plane displacement (perpendicular to the planes). The nodal displacements of one plane were fixed to the ground and those of the other plane were rigidly linked to the mid-plane slab by means of suitable tying-elements [44]. Therefore, it was likely to concentrate the frictional behavior between pavement and subbase in the interface elements (Figure 6b). The behavior is governed, in kinematic terms, by the bi-linear slippage law previously described in Section 2.2, which connects the in-plane interface relative displacements with the corresponding frictional shear stresses. Under a static point of view, the Mohr-Coulomb criteria was used for relating interface shear stresses to normal. A rather small influence of friction angle on slab behavior was stated by means of preliminary numerical analyses, since the slab is only loaded by its dead weight. Hence, a reference friction angle of thirty degrees was adopted together with a dilatancy angle of zero degrees; the latter was adopted in order to simulate an ideal perfect sliding condition. More in details, a gap criterion was also applied for describing gaps arising between slab and subbase as a result of a demand of tensile stresses normal to the subgrade. It was possible to easily take into account the stiffness of the subgrade ($K_{Winkler} = 0.08 \text{ N/mm}^3$), which is basically the elastic stiffness of the interface with respect to out-of-plane relative displacement (Figure 6b). A simplified scheme of the model adopted evidencing the rigid connection between plate and interface elements is shown in Figure 6b.

Each portion of jointless pavement investigated in the parametric study is identified by the notation, X-Y-Z-W, where: X represents the slab geometry ($20 = 20 \times 20 \text{ m}$ or $30 = 30 \times 30 \text{ m}$); Y the Glass-FRC (G05 = Glass-FRC05 or G10 = Glass-FRC10); Z the subgrade conditions (LF = low friction; HF = high friction); W the shrinkage distribution along slab thickness (Unifr, Lnr01 or Lnr02).

3.3. Validation of the Proposed Numerical Model

The numerical model adopted was verified by means of the analytical approach proposed by Zhang et al. [10,11], which refers to a simplified ideal beam element on continuum subbase in presence of a uniform shrinkage distribution along its cross-sectional depth. The frictional behavior between the beam and subbase is described by means of bi-linear laws. The model assumes a linear elastic behavior of concrete, both in compression and tension. In order to simulate the simplified beam geometry assumed by Zhang et al. [10,11], a slab 50 m long, 3 m wide, and 180 mm thick was considered. Basically, a long slab behaving like a beam element was considered; only one quarter was analyzed by taking advantage of the double symmetry, as schematically depicted in Figure 7a. The same basic hypotheses were applied with regard to concrete behavior, frictional subgrade properties (low friction) and shrinkage scenario. The latter was assumed uniform and equal to $110 \mu\text{m}/\text{m}$.

In Figure 7a the displacements distribution (along the longitudinal slab axis) resulting from the numerical model was reported and compared with the corresponding analytical predictions [10,11]. Similarly, in Figure 7b the distribution of shear stresses exchanged between slab and subgrade and axial slab stresses are compared to those stemming from the simplified approaches previously mentioned [10,11]. In this regard, suitable use of interface elements is fundamental for capturing the frictional effects at the contact surface between slab and subbase. A very good agreement between the numerical model and analytical method can be noticed, which confirms the reliability, even in a simple ideal condition, of the relatively simple model proposed herein. It is worthwhile underlining that analytical models able to take into account a possible non-uniform distribution of shrinkage strains along the slab thickness are not available in literature. Moreover, only in few research works [12,45] slabs-on-grade samples were deeply studied for studying shrinkage effects. Nevertheless, the aforementioned studies [12,45] were not considered for validating the numerical model because of the lack of information regarding the shrinkage strain distribution along the slab thickness, which is a parameter of paramount importance.

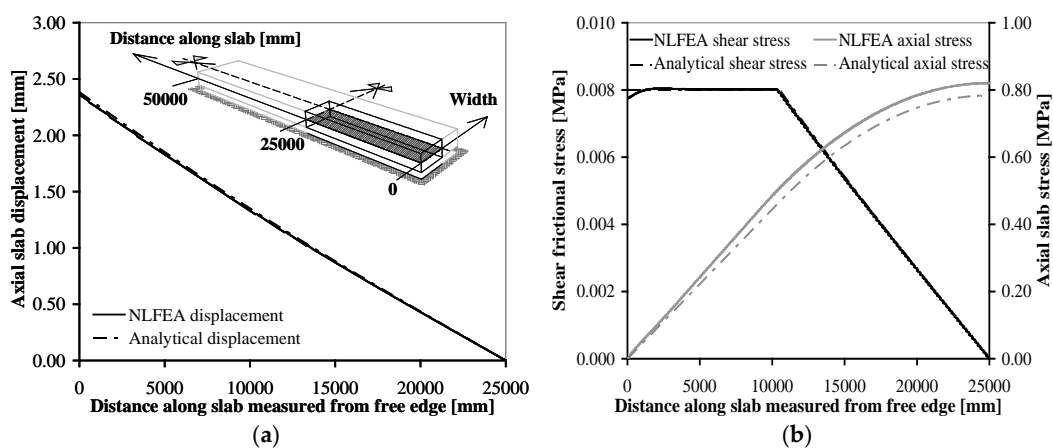


Figure 7. (a) Displacements along slab longitudinal axis; (b) axial slab stresses and shear stresses exchanged between slab and subbase.

4. Numerical Results

Numerical analyses were carried out by progressively increasing time steps for simulating the progressive development of shrinkage phenomena in the slab. The analyses were stopped when reaching almost the asymptotic value of imposed shrinkage strain (Figure 3) or when crack deformations tend to localize in specific regions of the slab and cannot be further controlled by glass fiber reinforcement. In the latter case, it means that in slab region where crack deformations tend to localize, the Glass-FRC post-cracking fracture energy (Figure 5) is almost completely exploited. Numerical results from 20-G10-LF-Lnr01 slab are extensively presented in this section. It should be

underlined that the shrinkage scenario Lnr01, based on the available literature [36], can be considered the most reliable. In the initial time steps, due to the free-shrinkage law adopted (Figure 3a), the autogenous shrinkage deformations are prevalent, mainly leading to a slab shortening and negligible curling effects (Figure 8a). The distribution of maximum principal stresses in slab mid-plane is reported in Figure 8b. It must be underlined that the stresses along the slab thickness do not vary because initially a small imposed curvature is introduced in slab-sections. Moreover, the degree of constraints due to the frictional effects at the slab-to-subgrade contact surface induces tensile axial stresses. The latter are maximum in the center region of the slab (Figure 8b) even though, in the early days, they are almost negligible stresses.

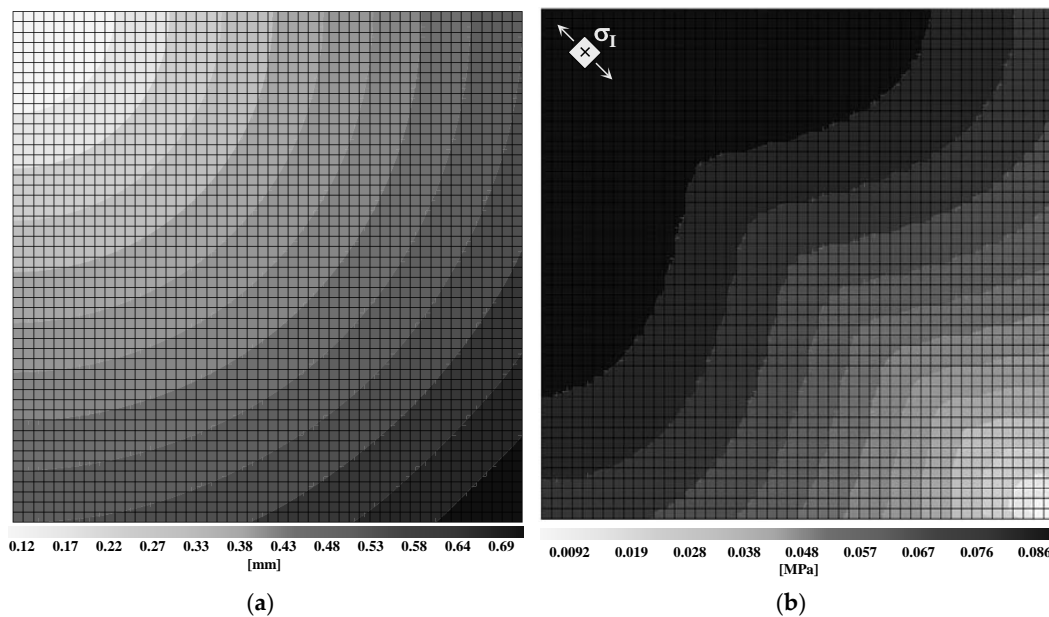


Figure 8. (a) Slab 20-G10-LF-Lnr01: displacements of slab mid-plane at 10 days; (b) maximum principal stresses of slab mid-plane at 10 days.

By increasing the time, the drying shrinkage distribution (Lnr01) strongly affects the slab behavior by inducing clear upward curling effects. The slab edges lift up and gaps arise between slab and subbase (Figure 9a). Even if the slab edges present an upward curvature, they tend to behave like a cantilever system because of their dead weight. Hence, tensile stresses result at the top surface of the slab in the center region of the pavement investigated (Figure 9a, maximum principal stresses at incipient cracking evidencing the slab upward curling). Accordingly, very small initial crack strains tend to arise in the central slab region.

By further studying the in-time crack development, the crack deformations tend to localize in a specific region, as evidenced in Figure 9b. By integrating the crack deformations exhibited in this region an estimation of the expected crack width can be achieved. The in-time development of maximum tensile stresses and estimated crack width are plotted in Figure 10a,b, respectively.

By referring to the shrinkage scenario Lnr01, all the other slab configurations have exhibited a similar trend. Table 3 summarizes the age of all the slabs when first cracking occurs; the latter can be considered a representative parameter of the risk of cracking (the earlier the crack appears the higher the risk of cracking). It is worthwhile noticing that, by considering the reference shrinkage scenario Lnr01, first cracking appears, as previously mentioned, in almost all the cases after 28 days. Based on the approach previously mentioned, the estimated final crack width is reported as well (Table 3), in order to quantify the ability of glass fiber reinforcement in controlling cracking phenomena. The time-step analyses were developed until the crack width does not further increase (over time). The latter condition can occur when the maximum constraint due to subgrade is reached or when

the applied free-shrinkage law approaches the asymptote. The results evidence the considerable influence of subgrade properties (Lnr01 scenario). In case of low friction conditions, the post-cracking residual strengths of Glass-FRC05 and Glass-FRC10 are able to limit the cracks to very low values, independently of the dimensions of the jointless pavement investigated (Table 3). On the other hand, in presence of high friction subgrade configuration, it is recommended to limit slab dimensions to portion having a side of 20 m and to use Glass-FRC with adequate toughness such as Glass-FRC10. In fact, slab 20-G10-HF-Lnr01 exhibits a final crack width rather small (0.2 mm). Nevertheless, the higher amount of fiber considered (Glass-FRC10) is also able to mitigate crack development in slab 30-G10-HF-Lnr01 (Table 3).

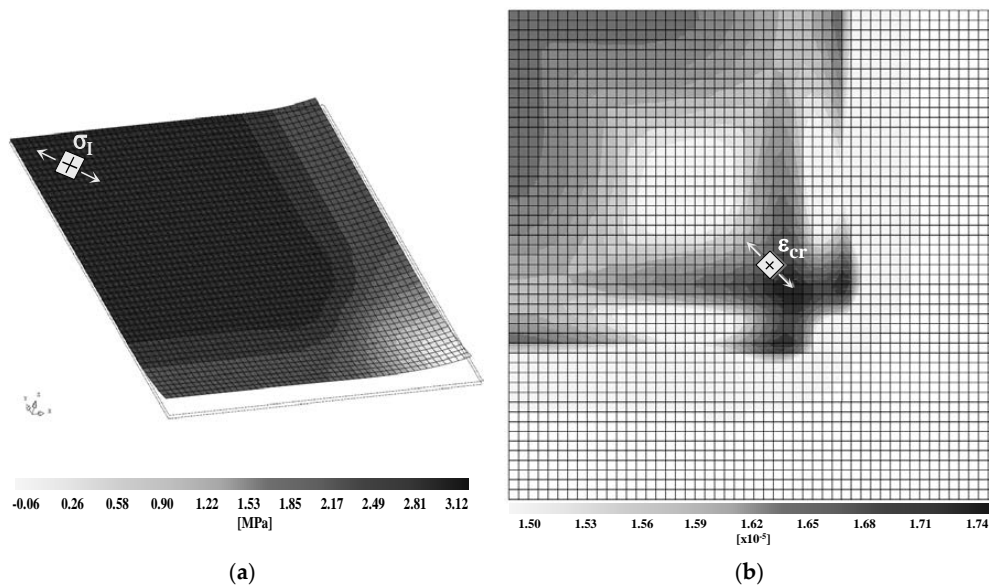


Figure 9. Slab 20-G10-LF-Lnr01: (a) deflected shape of slab mid-plane at 49 days with evidenced maximum principal stresses at top-slab-surface; (b) crack strain at top-slab-surface at 66 days.

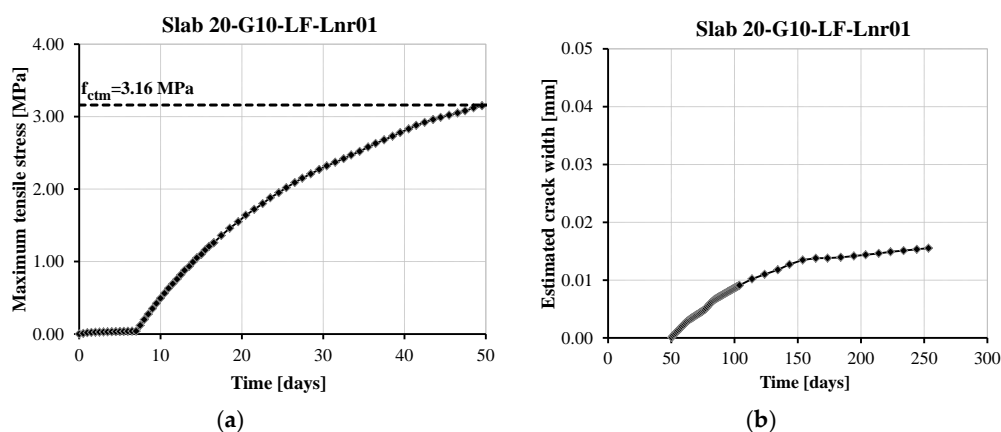


Figure 10. Slab 20-G10-LF-Lnr01: (a) maximum tensile stress in-time development; (b) estimated crack width in-time development.

By referring to the same age of the slab, besides the evaluation of crack width, the upward deflections of the free corner (T_z) have been reported in Table 3. T_z is a meaningful parameter since in Lnr01 condition, curling upward deflections occurred. All the slabs present similar upward deflections, with the exception of slab 30-G05-HF-Lnr01, which was not completely investigated due to difficulties in controlling crack development in such unfavorable conditions.

The shrinkage scenario Unifr and Lnr02 represents two kinds of lower and upper limits of the reference scenario Lnr01, respectively. In fact, in case of Unifr condition the slab behavior is completely governed by slab shortening, while in Lnr02 condition, upward curling effects arise earlier in the slab. The latter are noticeable as a result of the high imposed curvature and they are completely governing the slab behavior, leading to a much more severe localization of the cracking phenomena. In Figure 11, the effects of the different shrinkage scenarios investigated are presented for slabs 20-G10-LF. It can be noticed that, in case of Unifr slab, the tensile stresses are much lower than Lnr01 condition, resulting in the absence of cracks (Figure 11a). On the other hand, for Lnr02 configuration the stresses develop earlier determining a higher risk of cracking (Figure 11a). Similar tendencies can be found with reference to crack development (Figure 11b). Slab 20-G10-LF-Lnr02 presents much higher crack widths that those occurring in 20-G10-LF-Lnr01.

Table 3. Summary of main results exhibited by slabs in the post-cracking stage: scenarios Lnr01 and Lnr02.

Slab ID	First Cracking Age (days)	Estimated Crack		Upward Deflection of Free Corner, T_z (mm)
		Age (days)	Width (mm)	
20-G05-HF-Lnr01	35	294	0.592	8.2
20-G10-HF-Lnr01	35	294	0.200	8.3
30-G05-HF-Lnr01	25	78 ¹	0.626	5.3
30-G10-HF-Lnr01	25	294	0.906	8.7
20-G05-LF-Lnr01	49	244	0.014	9.3
20-G10-LF-Lnr01	49	253	0.016	9.4
30-G05-LF-Lnr01	43	223	0.020	9.0
30-G10-LF-Lnr01	43	194	0.017	8.7
20-G05-HF-Lnr02	22	303	0.850	9.2
20-G10-HF-Lnr02	22	324	0.767	13.5
30-G05-HF-Lnr02	18	39 ¹	0.661	5.8
30-G10-HF-Lnr02	18	46 ¹	0.488	7.0
20-G05-LF-Lnr02	28	324	0.918	10.8
20-G10-LF-Lnr02	28	294	0.560	13.0
30-G05-LF-Lnr02	26	251	1.080	12.4
30-G10-LF-Lnr02	26	331	0.570	13.5

¹ Not possible to study further time steps.

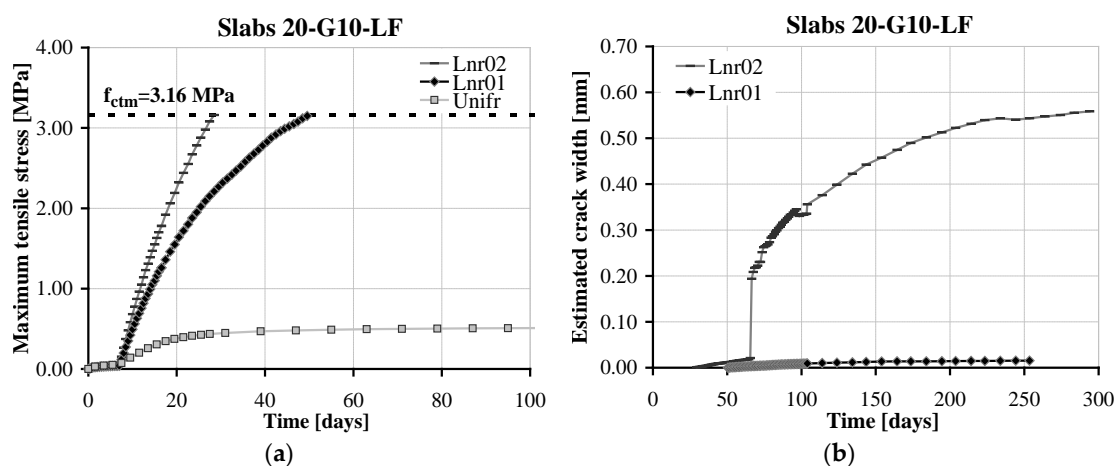


Figure 11. Effect of different shrinkage scenarios: (a) maximum tensile stress in-time development; (b) estimated crack width in-time development.

In all the slabs investigated with a uniform shrinkage distribution along the slab thickness, the risk of cracking was considerably limited. The corresponding maximum axial tensile stresses obtained from the time-step numerical analyses, are reported in Table 4. The stresses are indicated according to the global x and y in-plane slab directions ($\sigma_{X,max} = \sigma_{Y,max}$, since the maximum stresses were detected along the diagonal direction of the slab). In all slabs, the latter always remained below the concrete tensile strength (f_{ctm}) and no-cracks occurred. Moreover, in all cases $\sigma_{X,max}$ is almost constant after approximately 80 days. In fact, at a given imposed uniform shrinkage deformation, a noticeable axial slab shortening is imposed; hence, the global frictional constraint due to the subbase could not further increase and the slab tends to freely shrink. In this regard, the total in-plane axial displacement of the slab free corner (T_d) exhibited after one year, have been summarized in Table 4, for the uniform shrinkage. T_d is a meaningful parameter for describing the slab kinematic behavior in these cases. By considering the same slab dimensions, approximately the same values of T_d can be estimated, since, after about 80 days, all the slabs started to freely shrink, as mentioned before.

Eventually, even if the Unifr case is probably an ideal condition, it proves that, in the case of very low shrinkage gradient along the slab thickness, the risk of cracking considerably decreases. Nevertheless, the jointless pavement behavior, in terms of maximum tensile stresses, is governed by the axial slab shortening, leading to a great influence of the frictional subgrade properties. In fact, in the presence of a high friction subbase configuration, $\sigma_{X,max}$ are generally almost three times of those occurring in the presence of low friction (Table 4). These results underline the importance of the planarity of the subgrade as well as the need of a proper sliding plane under the concrete slab.

In case of shrinkage distribution Lnr02, as previously mentioned, a much higher tendency to localize cracking phenomena was observed in all the slabs investigated, generally leading to higher final crack widths, as summarized in Table 3. As an example, the corresponding crack strains distribution at top-slab-surface of slab 20-G10-LF-Lnr02 are reported in Figure 12a. Cracks tend to clearly localize along specific regions, which are almost delimiting the perimeter of the uplifted slab regions (Figure 12a). The higher is the tendency to localize crack strains in certain regions, the higher the estimated crack width, which can also present a sudden increase in its in-time development, as shown in Figure 11b for slab 20-G10-LF-Lnr02.

The higher demand in terms of crack control related to condition Lnr02 confirms that it is probably an upper-bound limit (based on data available in literature). Nevertheless, in this case, the different performances achievable by Glass-FRC10 slabs with respect to Glass-FRC05 ones, can be better appreciated. By comparing the crack development exhibited by slabs 20-G10-Lnr02 with 20-G05-Lnr02 (low and high friction, Figure 12b), it can be noticed an average decrease of about 40% of the final crack width when the higher fiber dosage is used. These results underline the need of a FRC material with a higher toughness when critical conditions in terms of friction at the subgrade interface are present.

Table 4. Summary of main results exhibited by slabs in the Unifr scenario: all slabs are un-cracked and the maximum stresses reached in-time constant values after about 80 days.

Slab ID	Maximum Tensile Stress	Axial Displacement of Free
	$\sigma_{X,max} = \sigma_{Y,max}$	Corner, $T_x = T_y$ (T_d)
	(MPa)	(mm)
20-G05-HF-Unifr	1.10	5.3 (7.5)
20-G10-HF-Unifr		
30-G05-HF-Unifr	1.63	7.9 (11.2)
30-G10-HF-Unifr		
20-G05-LF-Unifr	0.37	5.4 (7.6)
20-G10-LF-Unifr		
30-G05-LF-Unifr	0.57	8.1 (11.5)
30-G10-LF-Unifr		

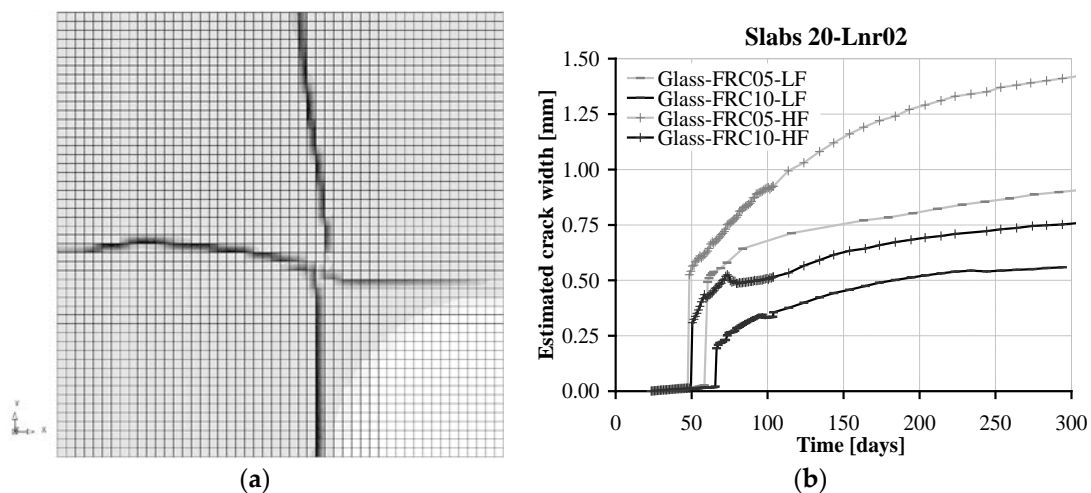


Figure 12. Slab 20-Lnr02 (a) crack strain at top-slab-surface at 66 days, low friction configuration; (b) effect of glass fiber reinforcement dosage on crack development.

Furthermore, diagrams in Figure 12b also evidence the influence of the frictional properties of the subgrade in case of high imposed curvature due to shrinkage (Lnr02). By comparing slabs 20-G10-HF-Lnr02 with 20-G10-LF-Lnr02 (or 20-G05-HF-Lnr02 with 20-G05-LF-Lnr02), an average increment of about 1.4 times of the final crack width is evidenced in case of high friction subbase conditions. Nevertheless, the effects of subgrade conditions were much less than those evidenced in case of Lnr01 shrinkage configuration. In fact, by comparing slabs 20-G10-HF-Lnr01 with 20-G10-LF-Lnr01, the final crack width is more than 10 times higher, when the unfavorable HF condition is considered. The latter phenomena is due to the noticeable curling effects introduced with Lnr02, that lead to a lifting of the slab in larger regions; hence, the effects of different subgrade frictional properties tend to diminish with respect to Lnr01 or Unifr cases.

By further analyzing the data summarized in Table 3, slabs 30-Lnr02 have generally presented much higher final crack widths. Moreover, slabs 30-HF-Lnr02 have exemplified particularly unfavorable conditions; the first cracking have occurred earlier and cracks have widened rapidly, leading to difficulties in controlling crack development by means of FRCs, as demonstrated by impossibility to complete the corresponding time-steps numerical analyses. Consequently, referring to slab conditions, with a high shrinkage gradient through the thickness of the jointless pavement, it is recommended to limit as much as possible the distance between construction joints. Moreover, is should be better prepared the subgrade in order to reduce friction (low friction) together with the adoption of FRCs having a higher post-cracking resistance.

In slabs under Lnr02 shrinkage configuration, the upward deflections (T_z) are generally higher than those exhibited by slabs under Lnr01 conditions (Table 3), as expected. As result to the great imposed curvature (Lnr02), rather discrete differences in T_z can be noticed when comparing the two amount of fiber reinforcement considered. By referring to the same slab dimensions and subgrade conditions, it can be noticed that the higher the toughness exhibited by Glass-FRC, the higher T_z is. In fact, Glass-FRC10 enables a better crack control than Glass-FRC05 and lower crack widths; thus, the corresponding slab planes where cracks localize (Figure 12a) tend to have smaller relative rotations when the free uplifted slab-edges are loaded by their dead weight. Consequently in Glass-FRC10 slabs, the free-edges show higher upward deflections. To the contrary, in Glass-FRC05 slabs, the onset of crack localization determines considerable rotations of the cracked planes. The latter phenomena is the main responsible of a kind of local rotational sag of the slab uplifted edge-regions, which tend to become more flat under their dead-weights, giving the impression of reduced curling. Similar trend was found by Banthia et al. [12] in experimental tests carried out on small scale slab specimens.

5. Conclusions

The present paper reports the main results from a non-linear numerical study of jointless industrial pavements reinforced with glass fibers, during shrinkage development before applying the external loads.

The floor is assumed as a slab on a Winkler soil; the numerical model is able to capture the concrete post-cracking behavior as well as frictional effects at the slab-to-subgrade contact-surface.

The main parameters studied for evaluating the risk of cracking phenomena are the following: the slab size (e.g., distance between construction joints), the friction at the subgrade interface, the shrinkage gradient through the slab thickness, and the FRC toughness.

Based on the results and the discussion presented, the main findings are the following:

1. The proposed relatively simple numerical model is able to provide a reliable prediction about the effects of shrinkage phenomena on jointless pavement, since it is based on a suitable application of interface elements for taking into account friction stresses arising between slab and subbase;
2. The slabs-on-grade behavior under shrinkage development is mainly governed by the interfacial friction between the slab and the supporting base. If the subgrade surface is not adequately prepared and a high friction is expected, it is recommended to limit the distance between construction joints and to use FRC with adequate toughness;
3. With a very high shrinkage gradient along the slab thickness, a higher risk of cracking was observed in all the slabs investigated, leading to generally higher final crack widths as well as higher curling upward deflections;
4. In case of very low variation of moisture demand through the thickness of the jointless pavement the risk of cracking considerably decreases. Nevertheless, since the behavior of the slab is governed by its axial shortening, a strong influence of the frictional properties of the subgrade on the maximum tensile stresses, was evidenced;
5. This parametric numerical study represents a useful tool that can be adopted for preliminary estimating cracking behavior of jointless pavements under shrinkage phenomena. This is important since in practice the latter is generally not directly considered in the design process, which is mainly focused only on the effects on pavements of the applied external loads.

Author Contributions: G.T., G.P. and B.B. designed the parametric study; G.T. and A.M. performed all the numerical analyses; G.T., A.M., G.P. analyzed the numerical results; G.T. and A.M. wrote the paper; G.P. reviewed the paper; G.T. and A.M. edited the final paper.

Funding: This study was funded by Owens Corning (Chambéry, France, grant number: 4508755118).

Acknowledgments: The Authors are thankful to Eng. Maria Novella Masotti for the assistance in performing non-linear FE analyses.

Conflicts of Interest: The authors declare no conflict of interest. The funders contributed in the design of the study but they had no role in the collection, analyses, or interpretation of data; in the writing of the manuscript, and in the decision to publish the results.

Notation List

E_c	concrete elastic modulus;
f_{cm}	mean cylindrical compressive concrete strength;
$f_{cm,cube}$	mean cubic compressive concrete strength;
f_{ck}	characteristic cylindrical compressive concrete strength;
f_{ctm}	mean cylindrical tensile concrete strength;
f_{Lm}	mean value of limit of proportionality;
f_{Ftsm}	mean value of post-crack strength for serviceability crack opening;
f_{Ftum}	ultimate residual strength (post-cracking strength for ultimate crack opening);
f_{Rjm}	mean residual flexural tensile strength of fiber reinforced concrete corresponding to $CMOD=CMOD_j$;
f_{uf}	ultimate tensile strength of fiber's filament;

h_0	notional size of structural element;
K_{Winkler}	Winkler soil stiffness;
L_f	fiber length;
L_f/φ_f	fiber aspect ratio;
L_i	internal length adopted in numerical analyses;
T_d	total in-plane axial displacement of slab free corner;
T_X	axial displacement in global x in-plane direction of slab free corner;
T_Y	axial displacement in global y in-plane direction of slab free corner;
T_Z	upward deflection of slab free corner;
V_f	volume fraction of fibers;
w_1	crack width at breakpoint (bi-linear post-cracking law);
w_c	ultimate crack width (bi-linear post-cracking law);
δ_0	relative displacement between subgrade and slab (end of elastic branch of bilinear function adopted);
$\varepsilon_a(t)$	autogenous shrinkage deformation at a given time (free shrinkage law);
$\varepsilon_d(t)$	drying shrinkage deformation at a given time (free shrinkage law);
σ_1	post-cracking tensile strength at breakpoint (bi-linear post-cracking law);
$\sigma_{X,\max}$	maximum axial slab stress in global x in-plane direction;
$\sigma_{Y,\max}$	maximum axial slab stress in global y in-plane direction;
τ_0	shear frictional stresses between subgrade and slab (end of elastic branch of bilinear function adopted);
φ_f	fiber diameter.

References

1. *Guide for Concrete Floor and Slab Construction*; ACI: Farmington Hills, MI, USA, 1996; p. 65.
2. *Design of Slabs on Grade*; ACI: Farmington Hills, MI, USA, 1997; p. 57.
3. Istruzioni per la progettazione, l'esecuzione ed il controllo delle pavimentazioni di calcestruzzo. Available online: <https://www.cnr.it/it/node/2631> (accessed on 4 September 2018).
4. British Concrete Society. *Concrete Industrial Ground Floors: A Guide to Design and Construction*; Technical Report; The Concrete Society: Camberley, UK, 2003; p. 140.
5. Barragan, B.; Facconi, L.; Plizzari, G.A. Design of glass fiber reinforced concrete floors according to the fib Model Code 2010. *ACI Spec. Publ.* **2014**, *310*, 311–320.
6. Suprenant, B.A. Why Slabs Curl Part I: A Look at the Curling Mechanism and the Effect of Moisture and Shrinkage Gradients on the Amount of Curling. Available online: <https://trid.trb.org/view/709544> (accessed on 4 September 2018).
7. Suprenant, B.A. Why Slabs Curl Part II: Factors Affecting the Amount of Curling. Available online: <https://trid.trb.org/view/710678> (accessed on 4 September 2018).
8. Ytterberg, R.F. Control of Shrinkage and Curling in Slabs on Grade Part I: Shrinkage Problems: Causes and Cures. Available online: https://www.google.com.hk/url?sa=t&rct=j&q=&esrc=s&source=web&cd=1&ved=2ahUKewi42PrF3aDdAhWZ7GEKHfytBsYQFjAAegQIAhAC&url=https%3A%2F%2Fwww.concreteconstruction.net%2F_view-object%3Fid%3D00000153-8bb4-dbf3-a177-9fbdce6d0000&usg=AOvVaw3dbxc0SwXUUApceQWHWBTd (accessed on 4 September 2018).
9. Ytterberg, R.F. Control of Shrinkage and Curling in Slabs on Grade Part II: How to Deal with Warping and Curling. Available online: https://www.concreteconstruction.net/_view-object?id=00000153-8bb3-dbf3-a177-9fbbd5390000 (accessed on 4 September 2018).
10. Zhang, J.; Leng, B. Analysis of shrinkage-induced stresses in concrete pavements. *Mag. Concr. Res.* **2004**, *56*, 585–595. [[CrossRef](#)]
11. Zhang, J.; Li, V.C. Influence of supporting base characteristics on shrinkage-induced stresses in concrete pavements. *J. Transp. Eng.* **2001**, *127*, 455–462. [[CrossRef](#)]
12. Banthia, N.; Bindiganavile, V.; Azhari, F.; Zantotti, C. Curling control in concrete slabs using fiber reinforcement. *J. Test. Eval.* **2014**, *42*, 390–397. [[CrossRef](#)]
13. Reggia, A.; Tortelli, S.; Marchi, M.; Borsa, M.; Plizzari, G.A. Analysis of a jointless floor with calcium sulpho-aluminate and portland cement. *ACI Spec. Publ.* **2015**, *305*, 45.

14. Mailvaganam, N.; Springfield, J.; Repette, W.; Taylor, D. Curling of Concrete Slabs on Grade. Available online: <http://citeseerx.ist.psu.edu/viewdoc/download?doi=10.1.1.6.178&rep=rep1&type=pdf> (accessed on 4 September 2018).
15. Garber, G. *Concrete Floors: Design and Construction of Concrete Floors*; Butterworth-Heinemann: Oxford, UK, 2006; p. 384.
16. Neal, F.R. *Concrete Industrial Ground Floors: ICE Design and Practice Guide*; Thomas Telford Publishing: London, UK, 2002; p. 62.
17. Meda, A.; Plizzari, G.A. New design approach for steel fiber-reinforced concrete slabs-on-ground based on fracture mechanics. *ACI Struct. J.* **2004**, *101*, 298–303. [[CrossRef](#)]
18. Sorelli, L.G.; Meda, A.; Plizzari, G.A. Steel fiber concrete slabs on ground: A structural matter. *ACI Struct. J.* **2006**, *103*, 551–558.
19. Falkner, H.; Huang, Z.; Teutsch, M. Comparative Study of Plain and Steel Fiber-Reinforced Concrete Ground Slabs. *Concr. Int.* **1995**, *17*, 45–51.
20. Tatnall, P.C.; Kuitenbouwer, L. Steel Fiber Reinforced Concrete in Industrial Floors. *Concr. Int.* **1992**, *14*, 43–47.
21. Vasaneli, E.; Micelli, F.; Aiello, M.A.; Plizzari, G. Long term behavior of frc flexural beams under sustained load. *Eng. Struct.* **2013**, *56*, 1858–1867. [[CrossRef](#)]
22. Tiberti, G.; Minelli, F.; Plizzari, G. Reinforcement optimization of fiber reinforced concrete linings for conventional tunnels. *Compos. Part B Eng.* **2014**, *58*, 199–207. [[CrossRef](#)]
23. Plizzari, G.A.; Cangiano, S.; Cere, N. Post-peak Behavior of Fiber-Reinforced Concrete under Cyclic Tensile Loads. *ACI Mater. J.* **2000**, *97*, 182–192.
24. Germano, F.; Tiberti, G.; Plizzari, G. Post-peak fatigue performance of steel fiber reinforced concrete under flexure. *Mater. Struct.* **2016**, *49*, 4229–4245. [[CrossRef](#)]
25. Nayar, S.K.; Gettu, R. A comprehensive methodology for the design of fibre reinforced concrete pavements. *ACI Spec. Publ.* **2014**, *310*, 321–330.
26. Wesevich, J.W.; McCullough, B.F.; Burns, N.H. Stabilized Subbase Friction Study for Concrete Pavements. Available online: <https://library.ctr.utexas.edu/digitized/texasarchive/phase2/459-1.pdf> (accessed on 4 September 2018).
27. Wimsatt, A.W.; McCullough, B.F.; Burns, N.H. Methods of Analyzing and Factors Influencing Frictional Effects of Subbases. Available online: <https://trid.trb.org/view/1182178> (accessed on 4 September 2018).
28. Rozycki, D.K.; Rasmussen, R.O. Assessment of Slab-Base Interaction in PCC Airfield Pavements. Available online: <https://trid.trb.org/view/506377> (accessed on 4 September 2018).
29. *Eurocode 2: Design of Concrete Structures—Part 1: General Rules and Rules for Buildings*; NSAI: Dublin, Ireland, 2004; p. 225.
30. *Test Method for Metallic Fibre Concrete—Measuring the Flexural Tensile Strength (Limit of Proportionally (LOP), Residual)*; BSI: London, UK, 2005; p. 18.
31. Brason, D.E. Shrinkage, Creep and Other Concrete Properties. In *Control of Cracking in Reinforced Concrete Structures: Research Project CEOS.fr (Civil Engineering and Geomechanics)*; Wiley-ISTE: London, UK, 2016; pp. 119–142.
32. ACI Committee. *Prediction of Creep, Shrinkage, and Temperature Effects in Concrete Structures*; American Concrete Institute: Farmington Hill, MI, USA, 1992; p. 47.
33. *CEB-FIP Model Code 1990*; Thomas Telford Publishing: London, UK, 1993; p. 437.
34. *Fib Model Code for Concrete Structures 2010*; Ernst & Sohn: Hoboken, NJ, USA, 2010; p. 434.
35. Rasmussen, R.O.; McCullough, B.F. *A Foundation for High Performance Jointed Concrete Pavement Design and Construction Guidelines*; Transtec Consultants: Austin, TX, USA, 1998.
36. Heath, A.C.; Roesler, J.R. Shrinkage and Thermal Cracking of Fast Setting Hydraulic Cement Concrete Pavements in Palmdale, California. Available online: <https://trid.trb.org/view.aspx?id=644231> (accessed on 4 September 2018).
37. Dere, Y.; Asgari, A.; Sotelino, E.D.; Archer, G.C. Failure prediction of skewed jointed plain concrete pavements using 3D FE analysis. *Fail. Anal.* **2006**, *13*, 898–913. [[CrossRef](#)]
38. Blanco, A.; Cavalaro, S.; De la Fuente, A.; Grunewald, S.; Blom, C.B.M.; Walraven, J.C. Application of FRC constitutive models to modelling of slabs. *Mater. Struct.* **2015**, *48*, 2943–2959. [[CrossRef](#)]

39. Bernardi, P.; Cerioni, R.; Michelini, E. Analysis of post-cracking stage in ssrc elements through a non-linear numerical approach. *Fract. Mech.* **2013**, *108*, 238–250. [[CrossRef](#)]
40. Diana v.9.4.4. Material Library Release. Available online: <https://dianafea.com/manuals/d944/MatLib/MatLib.html> (accessed on 4 September 2018).
41. Rots, J.G. Computational Modeling of Concrete Fracture. Ph.D. Thesis, Delft University of Technology, Delft, The Netherlands, September 1988.
42. Di Prisco, M.; Colombo, M.; Dozio, D. Fibre-reinforced concrete in fib Model Code 2010: Principles, models and test validation. *Struct. Concr.* **2013**, *14*, 342–361. [[CrossRef](#)]
43. Hillerborg, A.; Modéer, M.; Petersson, P.-E. Analysis of crack formation and crack growth in concrete by means of fracture mechanics and finite elements. *Cem. Concr. Res.* **1976**, *6*, 773–781. [[CrossRef](#)]
44. Diana v.9.4.4. Element Library Release. Available online: <https://dianafea.com/manuals/d944/ElmLib/ElmLib.html> (accessed on 4 September 2018).
45. Chen, H.L.; Schell, T.H.; Sweet, J.G. Field study of early-age behaviour of jointed plain concrete pavements. *ACI Spec. Publ.* **2002**, *206*, 243–258.



© 2018 by the authors. Licensee MDPI, Basel, Switzerland. This article is an open access article distributed under the terms and conditions of the Creative Commons Attribution (CC BY) license (<http://creativecommons.org/licenses/by/4.0/>).